Contrasting the Surface Phonon Dispersion of $Pb_{0.7}Sn_{0.3}Se$ in Its Topologically Trivial and Nontrivial Phases

S. Kalish, C. Chamon, and M. El-Batanouny

Department of Physics, Boston University, Boston, Massachusetts 02215, USA

L. H. Santos

Institute for Condensed Theory, University of Illinois at Urbana-Champaign, Urbana, Illinois 61801, USA
and Department of Physics, Emory University, Atlanta, Georgia 30322, USA

R. Sankar and F. C. Chou

Center of Condensed Matter Sciences, National Taiwan University, Taipei 10617, Taiwan

We report inelastic He atom scattering measurements of the (001) surface phonon dispersion of the topological crystalline insulator $Pb_{0.7}Sn_{0.3}Se$. This material exhibits a temperature-dependent topological transition, so we measure the surface dispersion curves in both the trivial and nontrivial phases. We identify that, peculiarly, most surface modes are resonances, rather than pure surface states. We find that a shear vertical surface resonance branch around 9.0 meV dramatically changes on going from the trivial to the topological phase. We associate this remarkable change with the emergence of surface Dirac fermions. We use the measured dispersion of this resonance branch to determine the corresponding mode-dependent electron-phonon coupling $\lambda_\nu(\mathbf{q})$.

Nontrivial topological crystalline insulator (TCI) phases are protected by an element or elements of its crystal symmetries and not by time-reversal symmetry as is the case of topological insulators (TIs). Both TIs and TCIs support metallic surface states while maintaining their bulk band insulating character. The presence of the metallic termination is dictated by a nontrivial $\mathbb{Z}_2$ bulk topological invariant in TIs [1–3], and by a mirror Chern number invariant [4–6] in the known TCIs, a property known as bulk-boundary correspondence. The topological invariants are associated with an intertwining of valence and conduction bands in the Brillouin zone that leads to a bulk band gap inversion at some high-symmetry points (time-reversal invariant momenta).

The IV-VI narrow gap semiconductor alloys $Pb_{1-x}Sn_xTe$ ($x \geq 0.3$) and $Pb_{1-x}Sn_xSe$ ($0.18 < x < 0.37$) [7] are the most-studied TCI systems [8–15]. They have also been extensively studied, including their bulk phonon dispersion, because of their attractive thermoelectric properties [16,17]. These systems have a rocksalt structure where the metallic surface states are protected by a $(1\bar{1}0)$ mirror-plane symmetry. The nontrivial surface states of topological $Pb_{1-x}Sn_x(Te, Se)$ exist on high-symmetry surfaces, such as (001), (110), and (111), that preserve the mirror symmetry with respect to the $(1\bar{1}0)$ bulk mirror planes. These narrow gap semiconductors have been known for decades to exhibit a wide range of electronic properties, such as ferroelectricity, superconductivity, and magnetism, to name a few. Such properties, as well as band gap inversion, can be easily tuned by alloying, doping, temperature, and strain [18]. Consequently, they have proliferated applications ranging from infrared lasers and detectors, to infrared optoelectronic and thermoelectric devices.

Although, in principle, the spin-orbit interaction (SOI) is not a prerequisite for obtaining a TCI, the TCI phase in $Pb_{1-x}Sn_x(Te, Se)$ compounds would not be achieved without the relativistic effects (SOI and Darwin term). Actually, SOI is responsible for the narrow band gap in these materials, which facilitates the process of band inversion. The band inversion in $Pb_{1-x}Sn_xSe$ occurs at the $L(111)$ points on the edge of the Brillouin zone. The direct band gap in PbSe is ∼0.29 eV, while the inverted band gap for Sn content $x \geq 0.3$ and $T \leq 195$ K is ∼0.1 eV [13]. A possible scenario is that the band inversion arises from the interplay of SOI and an asymmetric hybridization between cation and anion sp orbitals [19]. This scenario suggests that a topological phase transition could be achieved by applying external pressure or strain, which would directly affect the hybridization, as long as the mirror symmetries are preserved. It has been long recognized that the trivial phase has a valence band maximum with L_6^+ symmetry (mainly anion p character) and a conduction band minimum with L_6^- symmetry (mainly cation p character). This configuration appears in Pb(Se,Te), while the inverted phase shares the same symmetries with SnTe. Moreover,

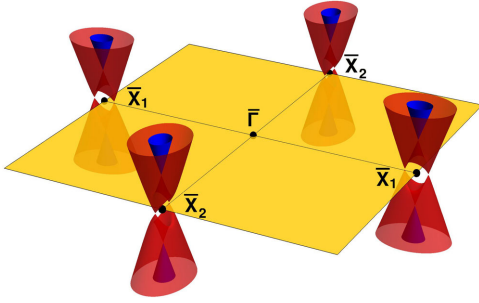FIG. 1.   Surface Brillouin zone with double-Dirac-cone structure.

FIG. 2.   Surface diffraction patterns along the (a) [10] and (b) [11] directions of the (001) rocksalt surface.

the presence of SOI endows the metallic surface states observed in these materials with spin-helicity textures.

Substitution of Sn for Pb in these alloys has two relevant effects. (i) It decreases the lattice constant a_0, approximately following Vegard's law for alloys [20–22]. The shrinking of the lattice is equivalent to applying an effective pressure with the concomitant effect of changing the degree of orbital hybridization [19]. (ii) It strongly changes the relativistic effects (Sn SOI is quite different from Pb) and results in a compositional evolution of their band structures, as evident in Refs. [12,13] for the selenide materials system. At appropriate temperatures, an increase in Sn content develops an effective bulk band gap closing at a specific critical alloy composition, followed by a band gap inversion where the parity of the electronic states at the band edges becomes reversed. In addition, for Sn content of $0.18 < x < 0.37$, a temperature-driven transition between a normal state and an inverted band gap state occurs at a critical temperature T_{top}.

Since both the (110) and (111) surfaces are not natural cleavage planes, we focus our work on the (001) surface. We find that two L points project onto the same $\bar{X}$ point of the surface Brillouin zone (SBZ), and each L point introduces a surface Dirac cone due to its band inversion. Hybridization of the two parent cones results in the characteristic double-Dirac-cone (DDC) structure, with two Dirac points (DPs) straddling the $\bar{X}$ point, and located slightly away from $\bar{X}$ along the $\bar{\Gamma}$-$\bar{X}$ direction, as shown in Fig. 1. The separation of the two DPs can be taken as a measure of this "hybridization." Since there are four $\bar{X}$ points on the SBZ boundary, there are four DDCs. The corresponding surface states form a new type of high-mobility chiral electron gas, which is robust against disorder and topologically protected by reflection symmetry of the crystal with respect to the $(1\bar{1}0)$ mirror plane.

Despite extensive research activities on many aspects of these TCIs over the past few years, experimental data on their surface dynamics and the interaction of surface phonons with the Dirac fermions (DFs) are scarce. An important requirement for topological insulators in device-oriented applications such as topological quantum information and low-power spintronics devices is the availability of dissipationless surface states in the topological regime.
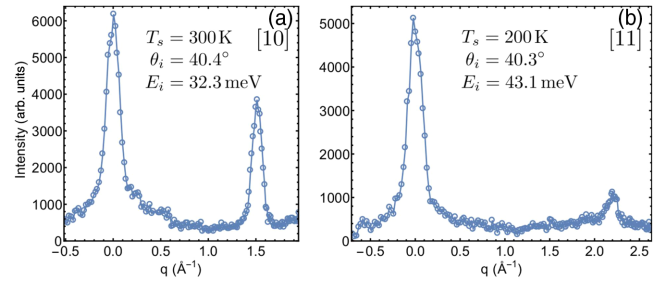
We address this outstanding aspect of the physics of TCIs in this Letter using inelastic He atom scattering (HAS) techniques. He atoms at thermal energies, employed in HAS, directly scatter from static and dynamic spatial modulation of the surface electron density about 2–3 Å away from the top surface atomic layer [23]. They experience no direct contact with surface or subsurface ion cores and are thus endowed with enhanced sensitivity to phonon-induced dynamic surface charge density (SCD) oscillations, even those induced by subsurface second-layer ionic displacements [24–26]. HAS intensities carry direct information about the SCD oscillations associated with surface phonons and ultimately about the surface electron-phonon interactions [27–29].

We performed extensive elastic and inelastic HAS measurements on the $Pb_{0.7}Sn_{0.3}Se$ (001) surface with He beam energies in the range 32–65 meV and a rotatable angle-resolved detector. Moreover, the samples were cleaved *in situ*. Measurements were performed at temperatures of 200 and 300 K, sufficiently below and above the critical temperature, $T_{\text{top}} \approx 250$ K, which characterizes the transition between the trivial and topological insulator phases for this Sn concentration [12,15]. Typical diffraction patterns along the [10] and [11] crystallographic directions are shown in Fig. 2. Diffraction measurements in the trivial and topological phases show no observable difference, which confirms the fact that the transition is only topological and there is no structural change. Inelastic spectra along the $\bar{\Gamma}$-$\bar{X}$ [30] direction are presented in Fig. 3 [35].

In order to interpret the inelastic experimental results, we used lattice dynamics calculations based on the shell model to fit available inelastic neutron data for bulk PbSe [36]. The results of this fitting are shown in Fig. 4. Of note is a large separation between the transverse-optical (TO) and longitudinal-optical (LO) branches at the Γ point, which indicates the presence of a large macroscopic electric field, and underscores the need to include long-range Coulomb interactions. This is implemented with the aid of Ewald-like summation [37]. The Sn alloying was incorporated via a virtual crystal approximation [38], primarily reflecting a change in the cation mass, and the results agree with trends observed in $Pb_{0.8}Sn_{0.2}Se$ data [39].

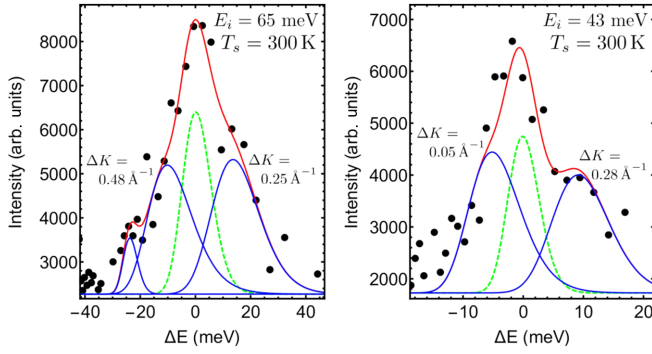FIG. 3. Two typical inelastic spectra along $\bar{\Gamma}$-$\bar{X}$ direction. The elastic peak is depicted as a dashed green line with incident beam energy width. Inelastic peaks are shown as solid blue lines with their corresponding ΔK as indicated.

In order to determine the surface phonon dispersion curves, we used a lattice dynamics slab geometry model of 120 atomic layers. The force constants obtained from the bulk fitting were incorporated in the slab calculations. The presence of DFs in the topological phase is accounted for by the addition of pseudocharges [29,40,41] in the three outermost layers, while maintaining charge neutrality. These pseudocharges represent the free-electron nature of the DFs, and the implied screening is accounted for by an explicit q dependence of the associated force constants, which effectively terminates beyond $2k_F$.

The projection of the bulk dispersion curves onto the $\bar{\Gamma}$-$\bar{X}$ direction of the SBZ is shown in Fig. 5(a). Modes presenting longitudinal, shear vertical (SV), and shear horizontal (SH) polarization are in blue, green, and red, respectively. The overlap of the bulk TO and longitudinal-acoustic curves results in a peculiar reduction of gaps in the projection onto the surface, leaving small gaps near the zone center at about 10 meV and the zone boundary at 7 meV. Consequently, we find that surface phonon modes are predominantly surface resonances rather than pure surface gap states.

Results of the slab calculations are shown in Figs. 5(b) and 5(c). The projected bulk modes as well as surface modes of SH polarization have been removed to avoid
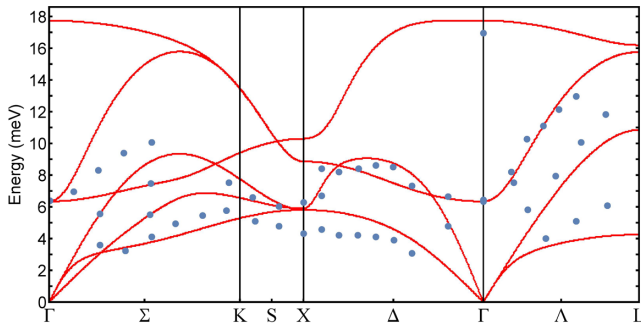

FIG. 4. Calculated PbSe bulk dispersion curves (red) fitted to available neutron data (blue) from Ref. [36].

clutter. In principle, surface SH modes are inaccessible to HAS in the sagittal plane; however the finite nature of the angle-resolving aperture may relax this constraint [42]. We do not find any overlap of our measured data with calculated SH modes. Calculated surface modes are shown in dark blue and dark green, while measured phonon events are depicted in orange with error bars. The results for the trivial phase are shown in Fig. 5(b). There is good agreement between the experimental results and predicted surface resonances of SV and longitudinal polarizations. The Rayleigh mode clearly appears at the bottom of the spectrum. However, of particular note is the nearly flat, weak SV resonance around 9.0 meV.

The results for the topological phase are shown in Fig. 5(c). In general, it replicates most of the features of the trivial phase, with minor modifications. The SV branch around 14 meV in the trivial phase is found to be a quite weak resonance and is seen to disappear in the topological phase as a result of the emergence of the surface DFs. However, the 9.0 meV SV resonance is now replaced with a new resonance, with the same polarization, that starts at 7.8 meV at the $\bar{\Gamma}$ point, and drops to a minimum of 5.8 meV at $q = 0.12$ Å^{-1}. This softening is due to DF screening arising from phonon-induced real transitions. We identify the 0.12 Å^{-1} value with $2k_F$ of the major axis of the DDC Fermi surface along the $\bar{\Gamma}$-$\bar{X}$ direction, which is consistent with the value of $k_F \approx 0.06$ Å^{-1} measured by angle-resolved photoemission spectroscopy [14,15]. We note that it is difficult to discern the effect of the minor axis with $2k_F \approx 0.08$ Å^{-1} on the phonon softening. For $q > 2k_F$, only virtual transitions survive and the screening is slowly suppressed, signaling a turnaround of the resonance dispersion curve towards higher frequencies. This resonance and the screening-induced softening in the range $q < 2k_F$ are reproduced in the slab calculations by the inclusion of surface pseudocharges and slight reduction of the surface force constants. These modifications were found to enhance the intensity of the resonance in the calculations. Moreover, the eigenvectors of this resonance branch obtained from lattice dynamics slab calculations show that it is predominantly associated with the motion of Se ions. This is consistent with the nature of strong electron-phonon interaction in an insulator such as $Pb_{1-x}Sn_xSe$, which comes from the coupling of the unscreened electric field of the optical phonon mode to the DFs [43]. Se is the lightest ion and has the largest amplitude of motion producing this electric field.

To extract information about the electron-phonon coupling, we use a microscopic model previously applied to the study of the interaction of surface DFs with surface phonons in the topological insulators Bi_2Se_3 [28] and Bi_2Te_3 [29]. The model is based on a linear Coulomb coupling of lattice ionic displacements to the DF density, which is incorporated in the phonon Matsubara Green's function,
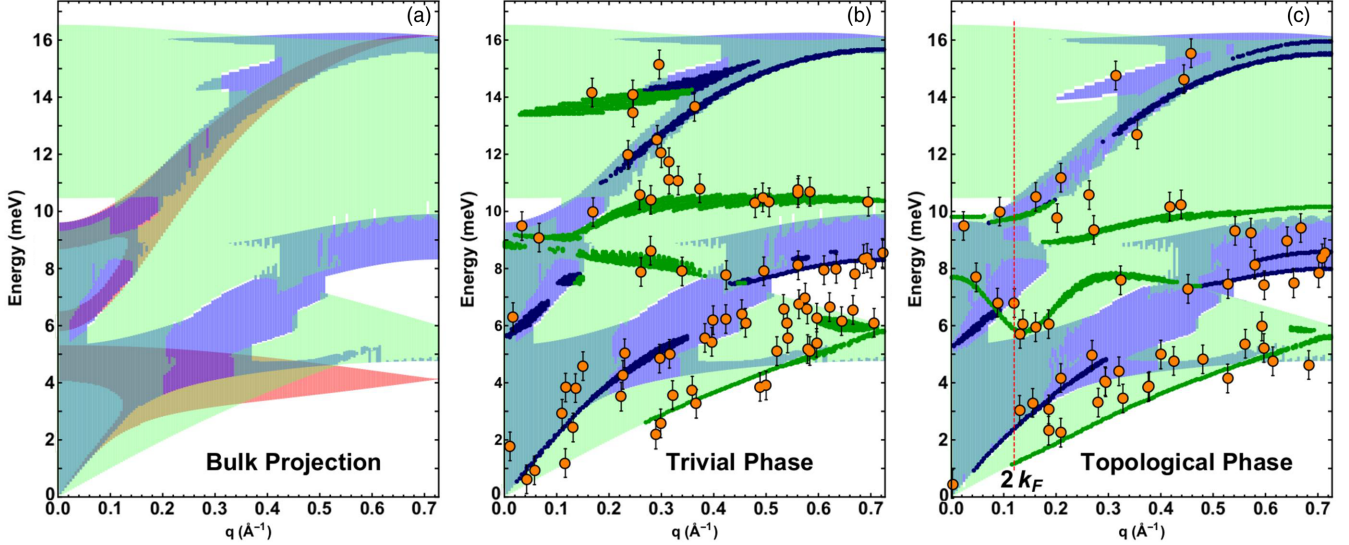
FIG. 5. (a) Bulk dispersion curves projected onto the $\bar{\Gamma}$-$\bar{X}$ direction of the surface Brillouin zone. Longitudinal polarization is shown in dark gray (blue). Shear horizontal polarization is shown in gray (red) and vertical shear polarization is shown in light gray (light green). (b) Surface dispersion curves in trivial phase regime. Calculated surface modes of longitudinal polarization are shown in black (dark blue) and those of shear vertical polarization are shown in dark gray (dark green). Measured phonon events are depicted as points with error bars (orange). (c) Surface dispersion curves in topological phase regime.

$$\mathcal{D}_\nu(\mathbf{q}, i\omega_n) = \frac{2(\hbar\omega_{\mathbf{q},\nu}^{(0)})}{(i\omega_n)^2 - (\hbar\omega_{\mathbf{q},\nu}^{(0)})^2 - 2(\hbar\omega_{\mathbf{q},\nu}^{(0)})\tilde{\Pi}}, \quad (1)$$

with

$$\tilde{\Pi} = |g_{\mathbf{q},\nu}|^2 \frac{\Pi(\mathbf{q}, i\omega_n)}{\epsilon(\mathbf{q}, i\omega_n)}, \quad (2)$$

where $g_{\mathbf{q},\nu}$ is the momentum and mode-dependent electron-phonon coupling. Π and ϵ are the electron polarization function and dielectric function of the DFs, respectively, calculated in the random phase approximation. In these calculations, we make a few simplifying assumptions [44]. First, because the surface phonon energies are small compared to the difference between E_F and the DDC saddle point, we consider only the region near the Fermi level. Locally, this has the structure of two concentric elliptic cones, as shown in Fig. 6. Second, the DDC of
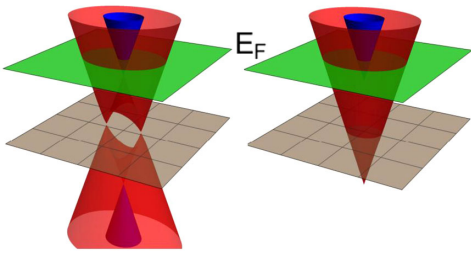

FIG. 6. Left: Double-Dirac-cone structure around $\bar{X}$ point. Right: Simplified elliptic cone used for electron-phonon calculation. The Fermi level is shown as green surface.

Pb$_{0.7}$Sn$_{0.3}$Se has elliptical Fermi surfaces, and the value of k_F is direction dependent. We performed a scaling transformation of the DF momentum axes that reduces the structure to a circular cone. This was done separately for the two orthogonal orientations of the DDCs at the two inequivalent $\bar{X}$ points.

The renormalized phonon frequencies are given by

$$(\hbar\omega_{\mathbf{q},\nu})^2 = (\hbar\omega_{\mathbf{q},\nu}^{(0)})^2 + 2(\hbar\omega_{\mathbf{q},\nu}^{(0)})\text{Re}[\tilde{\Pi}(\mathbf{q}, \omega_{\mathbf{q},\nu})]. \quad (3)$$

Fitting to measured phonon frequencies, shown in Fig. 7(a) is done through adjusting $\text{Re}[\tilde{\Pi}(\mathbf{q}, \omega_{\mathbf{q},\nu})]$. The value of the bare phonon frequency $\omega^{(0)}$ and k_F are extracted from our experimental and fitted results associated with the weak 9.0 meV resonance. A Kramers-Kronig transformation is then performed to obtain $\text{Im}[\tilde{\Pi}(\mathbf{q}, \omega_{\mathbf{q},\nu})]$ and determine the mode-dependent electron-phonon coupling $\lambda_\nu(\mathbf{q})$ using the relation [29,47,48]

$$\lambda_\nu(\mathbf{q}) = -\frac{\text{Im}[\tilde{\Pi}(\mathbf{q}, \omega_{\mathbf{q},\nu})]}{\pi\mathcal{N}(E_F)(\hbar\omega_{\mathbf{q},\nu})^2}, \quad (4)$$

where $\mathcal{N}(E_F)$ is the density of states at the Fermi surface. The calculated $\lambda_\nu(\mathbf{q})$ is shown in Fig. 7(b). Note that the small shoulder in $\lambda_\nu(\mathbf{q})$ corresponds to the shorter of the two elliptical axes of the Fermi surface.

We have measured the surface phonon dispersion of Pb$_{0.7}$Sn$_{0.3}$Se in both its trivial and topological phases. These measurements reveal a striking difference in the dispersion of a SV phonon resonance branch near 7.8 meV. Whereas it is almost flat in the trivial phase, screening by
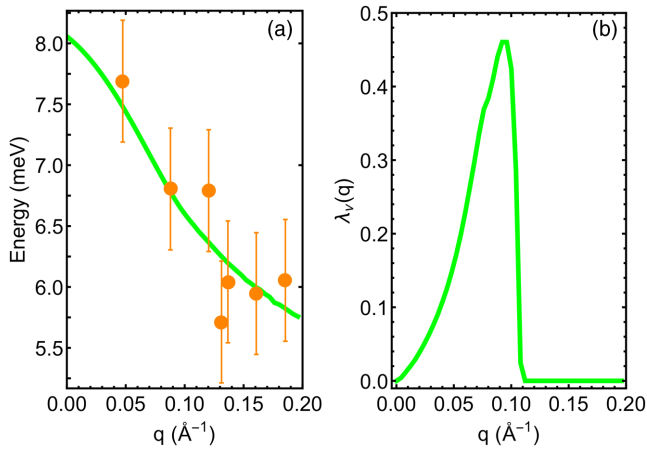
FIG. 7. (a) Renormalized surface phonon mode with measurements. (b) Mode-specific **q**-dependent electron-phonon coupling $\lambda_\nu(\mathbf{q})$.

the emerging DFs in the topological phase leads to softening and a monotonic decrease in frequency for $q \leq 2k_F$. Lattice dynamics calculations reproduce these effects via the introduction of surface pseudocharges. Finally, we determined phonon-mode-specific electron-phonon coupling by fitting a Matsubara Green's function model to the measured dispersion and using a Kramers-Kronig transformation to determine the corresponding linewidths.

[1] C. L. Kane and E. J. Mele, Phys. Rev. Lett. **95**, 146802 (2005).
[2] L. Fu and C. L. Kane, Phys. Rev. B **76**, 045302 (2007).
[3] L. Fu, C. L. Kane, and E. J. Mele, Phys. Rev. Lett. **98**, 106803 (2007).
[4] J. C. Y. Teo, L. Fu, and C. L. Kane, Phys. Rev. B **78**, 045426 (2008).
[5] L. Fu, Phys. Rev. Lett. **106**, 106802 (2011).
[6] J. Liu, W. Duan, and L. Fu, Phys. Rev. B **88**, 241303 (2013).
[7] Since PbSe has the cubic rocksalt structure, whereas SnSe has the orthorhombic B29 structure, these compounds do not form a complete series of pseudobinary solid solutions, and thus there is an upper limit of alloying.
[8] Y. Tanaka, T. Sato, K. Nakayama, S. Souma, T. Takahashi, Z. Ren, M. Novak, K. Segawa, and Y. Ando, Phys. Rev. B **87**, 155105 (2013).
[9] Y. Ando, J. Phys. Soc. Jpn. **82**, 102001 (2013).
[10] Y. Tanaka, Z. Ren, T. Sato, K. Nakayama, S. Souma, T. Takahashi, K. Segawa, and Y. Ando, Nat. Phys. **8**, 800 (2012).
[11] T. H. Hsieh, H. Lin, J. Liu, W. Duan, A. Bansil, and L. Fu, Nat. Commun. **3**, 982 (2012).
[12] B. M. Wojek, P. Dziawa, B. J. Kowalski, A. Szczerbakow, A. M. Black-Schaffer, M. H. Berntsen, T. Balasubramanian, T. Story, and O. Tjernberg, Phys. Rev. B **90**, 161202 (2014).
[13] P. Dziawa, B. J. Kowalski, K. Dybko, R. Buczko, A. Szczerbakow, M. Szot, E. Lusakowska, T. Balasubramanian, B. M. Wojek, M. H. Berntsen, O. Tjernberg, and T. Story, Nat. Mater. **11**, 1023 (2012).
[14] B. Wojek, M. Berntsen, V. Jonsson, A. Szczerbakow, P. Dziawa, B. Kowalski, T. Story, and O. Tjernberg, Nat. Commun. **6**, 8463 (2015).
[15] M. Neupane, S.-Y. Xu, R. Sankar, Q. Gibson, Y. J. Wang, I. Belopolski, N. Alidoust, G. Bian, P. P. Shibayev, D. S. Sanchez, Y. Ohtsubo, A. Taleb-Ibrahimi, S. Basak, W.-F. Tsai, H. Lin, T. Durakiewicz, R. J. Cava, A. Bansil, F. C. Chou, and M. Z. Hasan, Phys. Rev. B **92**, 075131 (2015).
[16] C.-C. Lin, G. Kim, D. Ginting, K. Ahn, and J.-S. Rhyee, ACS Appl. Mater. Interfaces **10**, 10927 (2018).
[17] Z. Tian, J. Garg, K. Esfarjani, T. Shiga, J. Shiomi, and G. Chen, Phys. Rev. B **85**, 184303 (2012).
[18] D. Khokhlov, Lead Chalcogenides: Physics and Applications (CRC Press, Boca Raton, FL, 2002), and references therein.
[19] P. Barone, T. Rauch, D. DiSante, J. Henk, I. Mertig, and S. Picozzi, Phys. Rev. B **88**, 045207 (2013).
[20] A. R. Denton and N. W. Ashcroft, Phys. Rev. A **43**, 3161 (1991).
[21] R. F. Bis and J. R. Dixon, J. Appl. Phys. **40**, 1918 (1969).
[22] A. Szczerbakow and H. Berger, J. Cryst. Growth **139**, 172 (1994).
[23] D. Farías and K.-H. Rieder, Rep. Prog. Phys. **61**, 1575 (1998).
[24] V. Chis, B. Hellsing, G. Benedek, M. Bernasconi, E. V. Chulkov, and J. P. Toennies, Phys. Rev. Lett. **101**, 206102 (2008).
[25] G. Benedek and J. Toennies, Surf. Sci. **299–300**, 587 (1994).
[26] G. Benedek, M. Bernasconi, V. Chis, E. Chulkov, P. M. Echenique, B. Hellsing, and J. P. Toennies, J. Phys. Condens. Matter **22**, 084020 (2010).
[27] A. Tamtögl, P. Kraus, N. Avidor, M. Bremholm, E. M. J. Hedegaard, B. B. Iversen, M. Bianchi, P. Hofmann, J. Ellis, W. Allison, G. Benedek, and W. E. Ernst, Phys. Rev. B **95**, 195401 (2017).
[28] X. Zhu, L. Santos, R. Sankar, S. Chikara, C. Howard, F. C. Chou, C. Chamon, and M. El-Batanouny, Phys. Rev. Lett. **107**, 186102 (2011).
[29] C. Howard, M. El-Batanouny, R. Sankar, and F. C. Chou, Phys. Rev. B **88**, 035402 (2013).
[30] Inelastic measurements were limited to the $\bar{\Gamma}$-$\bar{X}$ direction. See Supplemental Material at http://link.aps.org/supplemental/10.1103/PhysRevLett.122.116101 for explanation in Secs. III and V, which includes Refs. [31–34].
[31] Y. Ando and L. Fu, Annu. Rev. Condens. Matter Phys. **6**, 361 (2015), and references therein.
[32] A. Gyenis, I. K. Drozdov, S. Nadj-Perge, O. B. Jeong, J. Seo, I. Pletikosić, T. Valla, G. D. Gu, and A. Yazdani, Phys. Rev. B **88**, 125414 (2013).
[33] Y. J. Wang, W.-F. Tsai, H. Lin, S.-Y. Xu, M. Neupane, M. Z. Hasan, and A. Bansil, Phys. Rev. B **87**, 235317 (2013).

[34] M. Neupane, S.-Y. Xu, L. A. Wray, A. Petersen, R. Shankar, N. Alidoust, C. Liu, A. Fedorov, H. Ji, J. M. Allred, Y. S. Hor, T.-R. Chang, H.-T. Jeng, H. Lin, A. Bansil, R. J. Cava, and M. Z. Hasan, Phys. Rev. B **85**, 235406 (2012).

[35] See Supplemental Material at http://link.aps.org/supplemental/10.1103/PhysRevLett.122.116101 for a discussion of the fitting method in Sec. VI.

[36] P. Vijayaraghavan, S. Sinha, and P. Iyengar, Proc. Nucl. Phys. Solid State Symp. **16**, 208 (1973).

[37] F. W. de Wette and G. E. Schacher, Phys. Rev. **137**, A78 (1965).

[38] L. Nordheim, Ann. Phys. (Berlin) **401**, 607 (1931).

[39] L. Vodopyanov, I. V. Kutcherenko, A. Shotov, and R. Scherm, in *Lattice Dynamics*, edited by M. Balkanski (Flamarion, Paris, 1978), p. 673.

[40] C. S. Jayanthi, H. Bilz, W. Kress, and G. Benedek, Phys. Rev. Lett. **59**, 795 (1987).

[41] C. Kaden, P. Ruggerone, J. P. Toennies, G. Zhang, and G. Benedek, Phys. Rev. B **46**, 13509 (1992).

[42] A. Tamtögl, D. Campi, M. Bremholm, E. M. J. Hedegaard, B. B. Iversen, M. Bianchi, P. Hofmann, N. Marzari, G. Benedek, J. Ellis, and W. Allison, Nanoscale **10**, 14627 (2018).

[43] J. A. Sobota, S.-L. Yang, A. F. Kemper, J. J. Lee, F. T. Schmitt, W. Li, R. G. Moore, J. G. Analytis, I. R. Fisher, P. S. Kirchmann, T. P. Devereaux, and Z.-X. Shen, Phys. Rev. Lett. **111**, 136802 (2013).

[44] See Supplemental Material at http://link.aps.org/supplemental/10.1103/PhysRevLett.122.116101 for details in Sec. VII, which includes Refs. [45,46].

[45] V. Korenman and H. D. Drew, Phys. Rev. B **35**, 6446 (1987).

[46] E. Fradkin, E. Dagotto, and D. Boyanovsky, Phys. Rev. Lett. **57**, 2967 (1986).

[47] W. H. Butler, F. J. Pinski, and P. B. Allen, Phys. Rev. B **19**, 3708 (1979).

[48] X. Zhu, L. Santos, C. Howard, R. Sankar, F. C. Chou, C. Chamon, and M. El-Batanouny, Phys. Rev. Lett. **108**, 185501 (2012).